RSC Advances

ROYAL SOCIETY OF CHEMISTRY

www.rsc.org/advances

Graphical Abstract

Co_3O_4–CeO_2/SBA-15 monolith can efficiently filter and catalyze the soot particles. The optimized one exhibited a low T_{10} (293°C) and T_{90} (378 °C).

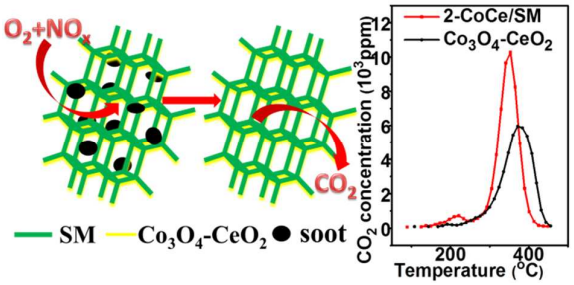

Co_3O_4–CeO_2 functionalized SBA-15 monolith with three-dimensional framework improves NO_x-assisted soot combustion

Qiongqiong Yang,[1,2] Fangna Gu,[2,*] Yufang Tang,[1,*] Hui Zhang,[2] Qing Liu,[2]

Ziyi Zhong,[3] and Fabing Su[2,*]

[1] *School of Chemical Engineering, Xiangtan University, Xiangtan 411105, Hunan, China*

[2] *State Key Laboratory of Multiphase Complex Systems, Institute of Process Engineering, Chinese Academy of Sciences, Beijing 100190, China*

[3]*Institute of Chemical Engineering and Sciences, A*star, 1 Pesek Road, Jurong Island, Singapore 627833, Singapore*

*Corresponding author: fngu@ipe.ac.cn (F. Gu), tyfchky@xtu.edu.cn (Y. Tang), fbsu@ipe.ac.cn (F. Su); Tel.: +86-10-82544850; Fax: +86-10-82544851

Abstract

In this work, cobalt and cerium composite oxides functionalized SBA-15 monolith (SM) with an inner three-dimensional (3D) network structure (CoCe/SM) were prepared by isovolumetric impregnation. Their catalytic activities towards NO_x-assisted soot combustion were evaluated and the loading and Co/Ce ratio were optimized. X-ray diffraction, scanning electron microscopy, energy dispersed spectroscopy, transmission electron microscopy, N_2 adsorption, X-ray photoelectron spectroscopy, H_2 temperature-programmed reduction and O_2 temperature-programmed desorption were employed to characterize the samples. It reveals that, compared with unsupported Co_3O_4–CeO_2 particles, the CoCe/SM catalysts with optimized Co_3O_4–CeO_2 loading show much higher catalytic ability, achieving a complete oxidation of the soot to CO_2 below 400 ^oC in the presence of NO_x, which are attributed to the high dispersion of Co_3O_4–CeO_2 on SM and the cross-linked macropore structure of SM that can house the soot particulate, thus providing closer contact between soot and catalytic active sites.

Keywords: Co_3O_4–CeO_2; 3D net-linked SBA-15; soot; NO_x; catalytic oxidation

1. Introduction

Diesel engines are of great importance to modern society and have been widely used in many sectors because of their high efficiency, low-operating costs, high durability and reliability. However, the emissions from the diesel engines contain soot and nitrogen oxides (NO_x), causing massive problems to the environment.[1] Various technologies have been developed to eliminate soot and NO_x, in which catalytic oxidation and diesel particulate filter are the two typical ways to remove soot,[2] while selective catalytic reduction (SCR) and lean NO_x traps (LNTs) are usually applied in NO_x control.[1] Since emitted pollutants from the diesel engine are usually a mixture of soot and NO_x, many researchers tried to use the NO_x-assisted soot combustion technology to simulate and evaluate the actual situation.[3, 4]

The reported catalysts for catalytic oxidation can be roughly classified as supported noble metals, perovskites and transition metal oxides. Although supported noble metal catalysts such as Ag supported on CeO_2,[5] Rh and Pt on La_2O_3,[4] Ag on TiO_2 and some other supported Pt and Pd catalysts[6] displayed outstanding catalytic activities for diesel soot combustion, however, they are quite expensive. The perovskite-type catalysts[3, 7-9] are thermal stable and low cost, and have high potential for simultaneous removal of soot and nitrogen oxides (NO_x), thus they have attracted high attention in these years.[6] For the transition metal oxides such as Mn-Ce,[10] Cu-Ce,[11] Co-Ce[12] mixed oxides, they are also catalytically active and may act as an effective alternative. Although these catalysts are generally cost-effective and show good catalytic activity to some extent, they often have very low surface areas, leading to their poor contact with the soot. To improve the contact between the catalysts and the soot, researchers usually put the active components on the cordierite monolith to act as a particulate filter.[13] However, the preparation process of this kind of filter is rather complicated; additionally, the active components on the filter are easy to fall off due to the

weak adhesion force between the monolithic support and the coating layer.

To overcome the above mentioned problems, recently we have worked on a new type of MnO_x–CeO_2/SBA-15 monolith catalysts for NO_x-assisted soot combustion.[14] Differing from the traditional monolithic catalysts, the SBA-15 monolith supported catalysts can be prepared more easily and free of any binder. Moreover, the high specific surface area of SM enables the high dispersion of active component on it for generation of more active sites, while the macropores derived from the 3D network in SM provide high accessibility of the soot reactants to the active sites. As demonstrated, the MnO_x–CeO_2/SBA-15 monolith catalysts could obviously reduce the initiation temperature of soot combustion. However, the combustion temperature window of soot is still relatively broad over it. Therefore, we have explored the possibility to further improve the performance of SBA-15 monolith catalysts for soot combustion by optimizing the active component in the catalysts.

Given the fact that ceria has a high oxygen storage capacity and well-known catalytic and redox properties (couples of Ce^{4+}/Ce^{3+}), which makes more oxygen available for the oxidation process, and the presence of mobile oxygen and weak Co-O bond in cobalt oxide as reflected in the relatively low ΔH for O_2 vaporization,[15] we have worked on the SM-supported Co_3O_4–CeO_2 (CoCe/SM) catalysts for soot combustion. In this work, different amounts of cobalt cerium composite oxides with a fixed Ce/Co ratio were impregnated on the 3D networked SBA-15 monolith to determine the most appropriate loading. The results reveal that, comparing with MnO_x–CeO_2/SBA-15 catalysts, the optimized CoCe/SM catalyst shows almost the same T_{10} (293 ^oC) but with a narrower temperature window of soot combustion and the T_{90} is only 378 ^oC.

2. Experimental

2.1. Catalyst preparation

The chemicals including citric acid monohydrate (CA H_2O), cerium (III) nitrate hexahydrate ($Ce(NO_3)_3$ $6H_2O$), cobalt(II) nitrate hexahydrate ($Co(NO_3)_2$ $6H_2O$) and anhydrous ethanol were from Sinopharm Chemical Reagent Co. Ltd., China, tetramethyl orthosilicate (TMOS) from Baishun Beijing Chemical Reagent Co. Ltd., China, and poly (ethylene oxide)-block-poly (propylene oxide)-block-poly (ethylene oxide) triblock copolymer (EO20PO70EO20, P123, M_{avg}=5800) from Sigma-Aldrich. All the above chemicals were of AR grade and used directly. The monolithic SBA-15 (SM) was synthesized according to the method described earlier.[16] Typically, 9.13 g TMOS was added dropwise to the already dissolved aqueous solution containing 6.89 g citric acid, 3.00 g P123 block copolymer and 112.00 g deionized water, and the mixture was kept under mild stirring till the monolith-like solid was formed at 313K for 24 h. The resulting gel was transferred into a teflon bottle and heated at 373K for 24 h. Subsequently, the solid product was recovered by filtration, washed with deionized water, and air-dried at room temperature. To remove the template, the dried monolithic solid was calcined in an air flow at 823K for 5 h in a tube furnace.

The cobalt and cerium oxides modified SM (CoCe/SM) with different Co_3O_4–CeO_2 loadings and Co/Ce ratios were prepared by isovolumetric impregnation. Firstly, the saturated adsorption capacity of SM was measured to be 9.8 g. Subsequently, 0.38 g $Co(NO_3)_2$ $6H_2O$ and 2.26 g $Ce(NO_3)_3$ $6H_2O$ were dissolved into 9.8 g anhydrous ethanol. The obtained clear solution was then added dropwise to 1 g SM support (10–20 mesh), sealed for 48 h, dried at room temperature, and then calcined at 773K for 5 h in a muffle furnace. The cobalt and cerium oxides modified SM (CoCe/SM) with the mass ratio of (Co_3O_4+CeO_2): SM at 1 and Co/Ce molar ratio at 1:4 was obtained and named as "1-$Co_{0.2}Ce_{0.8}$/SM". Likewise, other *n*-$Co_{0.2}Ce_{0.8}$/SM catalysts (*n* = 0.5, 2, 3 and 4) and 2-Co_xCe_y/SM (*x*:*y* is the molar ratio of Co/Ce) were prepared in the same way. In

addition, the Co_3O_4–CeO_2 with Co/Ce molar ratio at 1:4 was also synthesized by a citric acid-aided sol-gel method.[18]

2.2. Catalyst characterization

X-ray diffraction (XRD) patterns were recorded on a PANalytical X'Pert PRO MPD in the 2θ ranges of 0.6-5° and 20-90° using the Cu Kα radiation (λ=1.5418 Å) at 40 KV and 40 mA, and the patterns were checked with the card number of Joint Committee on Powder Diffraction Standards (JCPDS). N_2 adsorption isotherms at −196 °C were measured on a Quantachrome surface area & pore size analyzer NOVA 3200e. Prior to the measurement, the samples were degassed at 200 ℃ for 3 h under vacuum. The Brunauer-Emmett-Teller (BET) specific surface areas were calculated according to N_2 adsorption isotherms at the relative pressure range of 0.05−0.2. The pore size distribution (PSD) curve derived from the adsorption isotherm branch was calculated using the Barett-Joyner-Halenda (BJH) method. The scanning electron microscopy (SEM) images were measured on a JSM-7001F, JEOL, Tokyo, Japan for the observation of the morphologies of the samples, and the energy dispersed spectroscopy (EDS) (INCA X-MAX, JEOL, Oxford, England) was used to analyze the elemental composition. The transmission electron microscopy (TEM) measurements performed on a JEM-2010F, JEOL, Tokyo, Japan were applied to observe the microscopic features of the samples. X-ray photoelectron spectroscopy (XPS) was recorded using a VG ESCALAB 250 spectrometer (Thermo Electron, U.K.) with a nonmonochromatized Al Kα X-ray source (1486 eV) and the calibration of the binding energies was conducted using C1s peak at 284.6 eV as an internal standard. H_2 temperature-programmed reduction (H_2-TPR) was carried out on Quantachrome Automated chemisorption analyzer (chemBET pulsar TPR/TPD). Typically, 0.05 g sample was put into a quartz U-tube and pretreated at 300 °C in an Ar flow for 1 h and

subsequently cooled to room temperature. Afterwards, 10.0 vol% H_2/Ar gas flow with a flow rate of 50 mL min^{-1} was passed through the sample while the temperature was ramped to 1000 ^oC at a heating rate of 10 ^oC min^{-1}. A thermal conductivity detector (TCD) was applied to monitor the hydrogen consumption signal. Temperature programmed desorption of O_2 (O_2-TPD) was performed using 0.10 g catalyst loaded in a U-shaped quartz reactor on the Quantachrome chemisorption analyzer. The sample was firstly pretreated at 400 ^oC for 1 h under a He flow, followed by cooling down to 80 ^oC and maintained for 90 min under 5 vol % O_2/He with a gas flow of 40 mL min^{-1}. Subsequently, the sample was purged with a He flow for 1 h to remove the physically adsorbed O_2 and then heated to 950 ^oC at a heating rate of 10 ^oC min^{-1}. The outlet gas was analyzed by a thermal conductivity detector.

2.3. Catalytic activity measurement

The catalytic activities of the catalysts for soot combustion were evaluated through a temperature-programmed oxidation reaction (TPO) in a fixed-bed reactor from 100 to 650 ^oC at a heating rate of 2 ^oC min^{-1}.[14] Printex-U (Degussa) was used as the model soot, which has the average particle size of 25 nm and specific surface area of 100 m^2 g^{-1}. The supported catalyst or SM (200 mg, 10-20 mesh) and soot (10 mg) at a mass ratio of 20:1 were added in 15 ML anhydrous ethanol and subsequently treated by an ultrasonic irradiation at 40 KHz for 5 minutes to ensure a high dispersion of the soot into the macropores of the catalysts. The resulting mixture was then dried in an oven and transferred into the reactor. 1000 ppm NO/10% O_2/Ar (or only O_2/Ar) with a total flow rate of 50 mL min^{-1} was passed through the reactor. The composition of the outlet gas was analyzed by an on-line micro gas chromatograph (3000A; Agilent Technologies) equipped with two TCD detectors. The concentration of CO_2 was detected by the TCD detector with a Plot Q

column while the concentration of CO was analyzed by the other TCD detector with a molecular sieve column. The catalytic activity was evaluated by the temperature values of T_{10}, T_{50} and T_{90}, at which 10, 50 or 90% of soot conversion was achieved, respectively.[12] In detail, the soot TPO curve of a reaction was integrated, and the integral area was regarded as the total amount of soot in the reaction, the temperatures at which the integral areas reached 10, 50 or 90% of the total area corresponded to the T_{10}, T_{50} and T_{90}, respectively. Meanwhile, the selectivity to CO_2 (S_{CO_2}) formation was defined as the total molar ratio of $CO_2/(CO_2+CO)$ in the outlet gas during soot oxidation process.

3. Results and discussion

3.1. N_2-physisorption

Fig. 1a illustrates the nitrogen adsorption results of all the samples. SM exhibits type IV isotherms with a type-H1 hysteresis loop, attributing to the typical cylindrical channel of mesoporous material.[19] 0.5-$Co_{0.2}Ce_{0.8}$/SM also shows a Type IV isotherm; however, its hysteresis loop slightly tends to H2-type, which is usually attributed to the presence of "ink-bottle" like channels caused by the accumulation of little amount of composite oxides on one end of the channel. This phenomenon becomes more obvious in 1-$Co_{0.2}Ce_{0.8}$/SM. Moreover, with the increase of the Co-Ce oxide loading, the hysteresis loops of the supported catalysts become smaller in dimension, indicating that the pore volumes of the *n*-$Co_{0.2}Ce_{0.8}$/SM catalysts are gradually decreased. The isotherm of Co_3O_4–CeO_2 has a hysteresis loop of type H2, characteristic of the porous structure. The pore size distribution (PSD) curves derived from the adsorption branches using the BJH model are displayed in Fig. 1b. It can be seen that both SM and the supported catalysts have a narrow pore-size distribution with the most probable value of 7.7 nm, larger than that of Co_3O_4–CeO_2. In addition, from Table 1 it is seen that

the surface areas and pore volumes of *n*-$Co_{0.2}Ce_{0.8}$/SM catalysts are larger than that of Co_3O_4–CeO_2. Both the specific surface areas and pore volumes of *n*- $Co_{0.2}Ce_{0.8}$/SM catalysts are decreased with the increase of *n* value, indicating the Co-Ce mixed oxides are mainly deposited in the mesoporous channels of SM and/or accumulated on the outer surface of SM.

3.2. SEM observation

The SEM image and photograph (inset) of the SM support are shown in Fig. 2a. The inset of Fig. 2a shows that the SM support has a cylinder-like shape which is the same as that of the reactor. The SEM images reveal that the fiber-like components within SM are parallel-aligned and cross-linked with each other to form a periodically arranged framework in three dimensions throughout the whole sample. In addition, the network windows have a diameter of 1-6 μm, which can be controlled by adjusting the synthesis parameters such as the acid concentration, silica source amount, reaction time and aging condition.[16] For all the *n*-$Co_{0.2}Ce_{0.8}$/SM catalysts, the 3D frameworks within SM are still well preserved. Fig. 2b-d show that the outer surface of the fibers within SM is still relatively smooth at low Co_3O_4–CeO_2 loadings (*n*=0.5, 1, 2), suggesting that these Co_3O_4–CeO_2 particles are mostly distributed in the inner walls of SBA-15 mesoporous channels or highly dispersed on the outside surface of SBA-15 fibers. With further increase of the Co_3O_4–CeO_2 loading, the outer surface of the SBA-15 framework becomes rough, or accompanies with appearance of even large particles (Fig. 2e and 2f), indicating that the excess of Co_3O_4–CeO_2 will accumulate on the outer surface of SBA-15 fibers and agglomerate into large particles. Clearly, to ensure that the Co_3O_4–CeO_2 particles are highly dispersed on the support, the *n* value is better to be controlled at between 2 and 3.

The elemental mappings of 2-$Co_{0.2}Ce_{0.8}$/SM in Fig. 3 demonstrate that both Co and Ce are

present and homogeneously dispersed on the SBA-15 framework. In addition, the atomic percentages of Co and Ce are 4.27 and 14.10%, respectively, which can be translated to a Ce/Co ratio of 3.3, lower than the nominal value of 4.0, indicating the enrichment of Co on the surface.[20] This may be explained by the possibility that some small CeO_2 particles can enter into the mesoporous channels of SBA-15, while the Co_3O_4 particles cannot, mainly because of the too large crystal size (14 nm) of the later, as shown in Table 1.

3.3. TEM

The TEM images of SM and *n*-$Co_{0.2}Ce_{0.8}$/SM are displayed in Fig. 4. It can be seen that the SBA-15 fibers have ordered parallel channels with a diameter of about 8 nm (Fig. 4a). The TEM image of 0.5-$Co_{0.2}Ce_{0.8}$/SM in Fig. 4b shows that the Co_3O_4–CeO_2 particles about 5nm in size are highly distributed within the SBA-15 channels. For 2-$Co_{0.2}Ce_{0.8}$/SM, the dispersion of the oxide particles is still high but some large particles appear (Fig. 4c). Further increasing the Co_3O_4–CeO_2 loadings results in the formation of large particles accumulated on the external surface of the SBA-15 fibers, which is evidenced by the TEM images of 3-$Co_{0.2}Ce_{0.8}$/SM and 4-$Co_{0.2}Ce_{0.8}$/SM (Fig. 4d-e). These results agree with the above SEM observations shown in Fig. 2. The observed lattice distance of 0.32 nm in Fig. 4f is assigned to the (111) facet of CeO_2, while those of ca. 0.21 nm and 0.28 nm to the (400) and (220) facets of Co_3O_4, implying the coexistence of CeO_2 and Co_3O_4 in 3-$Co_{0.2}Ce_{0.8}$/SM.

3.4. XRD

Fig. 5 shows the XRD patterns of SM and *n*-$Co_{0.2}Ce_{0.8}$/SM. The low-angle XRD pattern of SM in Fig. 5a has three diffraction peaks indexed as (100), (110) and (200) plane respectively,

corresponding to the well-ordered meso-structure with a 2D symmetry (*p*6*mm*).[21] These three peaks almost disappear in the low-angle XRD patterns of the *n*-$Co_{0.2}Ce_{0.8}$/SM catalysts except for 0.5-$Co_{0.2}Ce_{0.8}$/SM which remains (100) plane, indicating the decrease of ordered degree due to the occupation of the SBA-15 channels by Co_3O_4–CeO_2 particles, which is consistent with the results of N_2 adsorption and TEM analysis. The wide-angle XRD patterns of Co_3O_4–CeO_2 and the *n*-$Co_{0.2}Ce_{0.8}$/SM (Fig. 5b) show the typical diffraction peaks of fluorite-like structure of CeO_2 (JCPDS Card No.00-034-0394) and several weak peaks of Co_3O_4 (JCPDS Card No.00-042-1467) except for 0.5-$Co_{0.2}Ce_{0.8}$/SM, which may be due to the high dispersion of Co_3O_4, and/or the too low cobalt oxide content to be detected by XRD instrument. In addition, the crystal sizes of Co_3O_4 and CeO_2 calculated by Debye Scherrer equation are listed in Table 1. It is seen that the crystal sizes of Co_3O_4 particles in *n*-$Co_{0.2}Ce_{0.8}$/SM are larger than 12 nm, while those of CeO_2 particles are 5.1 ~ 9.0 nm.

3.5. XPS

Fig. 6 shows the XPS spectra of 2-$Co_{0.2}Ce_{0.8}$/SM and Co_3O_4–CeO_2. The full-range spectrum in Fig. 6a demonstrates that all the anticipated elements (Co, Ce, O, Si) exist in the two catalysts. XPS spectrum of Co 2p in Fig. 6b consists of a spin-orbit doublet of Co $2p_{1/2}$ and Co $2p_{3/2}$. The spectrum of Co_3O_4–CeO_2 exhibits two distinct peaks at 780.5 eV for $2p_{3/2}$ and at 795.8 eV for $2p_{1/2}$ respectively, and another satellite peak at 786.5 eV. These features are characteristics of Co_3O_4.[22] This is consistent with the above wide-angle XRD results. Compared with those in bulk Co_3O_4–CeO_2, the peaks of Co $2p_{3/2}$ and Co $2p_{1/2}$ in 2-$Co_{0.2}Ce_{0.8}$/SM appear at higher binding energies, indicating the increase of Co^{2+} in the later.[12]

Fig. 6c shows the Ce 3d XPS spectra of 2-$Co_{0.2}Ce_{0.8}$/SM and Co_3O_4–CeO_2. The curves of Ce 3d

spectra are composed of eight peaks corresponding to four pairs of spin-orbit doublets. The peaks located at 885.8 eV (V') and 903.8 eV (U') are originated from Ce^{3+} species, while the other pairs at 882.5 (V) and 901.2 (U), 889.0 (V'') and 907.6 (U'') , 898.6 eV (V''') and 916.8 (U''') eV are attributed to Ce^{4+} species.[23, 24] The value of R_1 (the molar ratio of the Ce^{3+} to Ce^{4+}) in Table 2 reveals that Ce^{4+} ion is the predominant Ce species on the surface of the two catalysts. Comparing with Co_3O_4–CeO_2, 2-$Co_{0.2}Ce_{0.8}$/SM has higher R_1 value or larger amount of Ce^{3+} (Table 2), implying the presence of more oxygen vacancies in 2-$Co_{0.2}Ce_{0.8}$/SM,[25] which can enhance oxygen mobility[26] on the surface of the catalyst, thus conducive to the soot oxidation.

As shown in Fig. 6d, the O 1s spectrum of the Co_3O_4–CeO_2 oxides can be fitted into two peaks located at 529.1 and 531.6 eV assigned to the lattice oxygen (O^{2-}) and the adsorbed oxygen (O_2^- and O^-), respectively.[27] The two peaks of 2-$Co_{0.2}Ce_{0.8}$/SM move to higher binding energies in comparison with those of the Co_3O_4–CeO_2 oxides. What's more, the value of R_2 (the molar ratio of the adsorbed oxygen (O^-, O_2^-) to lattice oxygen (O^{2-})) shown in Table 2 is increased from 0.471 to 1.17 after supporting Co_3O_4–CeO_2 on SM. It may be because the introduction of SM can facilitate the high dispersion of the Co_3O_4–CeO_2, leading to the formation of much more exposed and efficient active sites, which can generate and carry more activated adsorbed oxygen (O^-, O_2^-) species for improvement of the catalytic activity for soot oxidation.

3.6. H_2-TPR and O_2-TPD

Fig. 7a displays the H_2-TPR profiles of all the catalysts. The reduction peaks are attributed to the reduction of Co_3O_4–CeO_2 mixed oxides within the testing temperature range since the SM support is hardly to be reduced. For 0.5-$Co_{0.2}Ce_{0.8}$/SM, the H_2 consumption peaks are relatively weak and merged together. In this sample, the metal oxide content is low, so most of the particles are

distributed in the SBA-15 channels, and probably these particles have strong interaction with the SBA-15 support. For 1-$Co_{0.2}Ce_{0.8}$/SM, it exhibits two reduction peaks at 355 and 430 ^{o}C, respectively. The former is assigned to the reduction of Co^{3+} to Co^{2+} while the later to the reduction of Co^{2+} to Co.[28, 29] For 2-$Co_{0.2}Ce_{0.8}$/SM, its reduction profile is very similar to that of 1-$Co_{0.2}Ce_{0.8}$/SM, because both of them have similar metal oxides dispersion on the support. However, in 2-$Co_{0.2}Ce_{0.8}$/SM, its reduction peaks move to lower temperature range, probably because of a weakened interaction between the metal oxides and the support. For 3-$Co_{0.2}Ce_{0.8}$/SM, it shows a weak peak at 355 ^{o}C, which may be attributed to direct reduction of small amount of free-standing Co_3O_4 to metallic Co. As reported, this kind of phase is able to dissociate hydrogen.[30] The subsequent reduction process is probably promoted by the hydrogen spillover effect thus a sharp peak centered at 380 ^{o}C is appeared. At high loadings, the Co_3O_4–CeO_2 particles start to aggregate on SM and become large particles. The reduction profile of 4-$Co_{0.2}Ce_{0.8}$/SM is similar to that of 3-$Co_{0.2}Ce_{0.8}$/SM except a slight shift of the reduction peaks to higher temperature. In contrast to the supported catalysts, the reduction peaks of unsupported Co_3O_4–CeO_2 move to higher temperature. In addition, the supported catalysts show another reduction peak at around 760 ^{o}C, which is attributed to the reduction of bulk CeO_2. This peak shifts to lower temperature compared with that of unsupported Co_3O_4–CeO_2 (800 ^{o}C), probably because of the higher dispersion and smaller size of CeO_2 particles on the SM. As reported, the proper loading of Co_3O_4–CeO_2 (e.g. 2-$Co_{0.2}Ce_{0.8}$/SM) on SM can enhance the dispersion of Co_3O_4–CeO_2 and weaken the interaction between the metal oxides and the SM, thus improving the redox ability[28] and surface oxygen mobility,[31] which is helpful to the soot oxidation.

In order to get further insight into the adsorption and activation behavior of the catalysts towards oxygen, O_2-TPD measurements were carried out and the results are shown in Fig. 7b. For all the

catalysts, the desorption peaks of adsorbed molecular O_2 are not observed, which may be due to the rapid activation of adsorbed oxygen molecular. Co_3O_4–CeO_2 shows only one steep peak centered at about 840 ^oC, which is attributed to the liberation of lattice oxygen (O^{2-}).[14,27] For *n*-$Co_{0.2}Ce_{0.8}$/SM (*n*=1, 2, 3, 4) catalysts, they show similar O_2-TPD profiles: a broad peak in the range of 500–750 ^oC assigned to the desorption of surface active oxygen species (O_2^- and O^-), and an intensive peak centered at about 835 ^oC due to the liberation of lattice oxygen (O^{2-}). However, with the increase of Co-Ce loadings, the peak areas in the range of 550-750 ^oC for *n*-$Co_{0.2}Ce_{0.8}$/SM (*n*=1, 2, 3, 4) are decreased gradually while those of the peaks centered at 835 ^oC become larger, indicating the decrease of the surface active oxygen species (O_2^-, O^-) amount but the increase of the lattice oxygen (O^{2-}) content. For 0.5-$Co_{0.2}Ce_{0.8}$/SM, it exhibits only a broad peak within 540-940 ^oC, indicating that the desorption species are mainly chemisorbed surface active oxygen species (O_2^-, O^-), because the Co_3O_4–CeO_2 is highly dispersed in this sample. Comparing with that of Co_3O_4–CeO_2, the desorption peaks of all the supported catalysts move to lower temperature range, indicating a better oxygen mobility. In short, low loading of Co_3O_4–CeO_2 on SM is unable to offer enough oxygen species demanded for the soot oxidation reaction; while too higher oxide loading results in the aggregation of Co_3O_4–CeO_2 on SM surface. Only in the case where Co_3O_4–CeO_2 is appropriate, e.g., 2-$Co_{0.2}Ce_{0.8}$/SM, the catalyst is able to work well for the soot combustion reaction.

3.7. Soot-TPO reactions

The catalytic activities of Co_3O_4–CeO_2 and *n*-$Co_{0.2}Ce_{0.8}$/SM for soot oxidation under NO/O_2 atmosphere were evaluated and the results are shown in Fig. 8a and Table 3. For comparison, the TPO reaction of the bare soot was also carried out and its T_{10}, T_{50}, T_{90} and S_{CO_2} (%) are 447, 563, 612 ^oC and 55%, respectively. Table 3 shows that SM has negligible catalytic activity towards

NO_x-assisted soot combustion. All the catalyst can promote soot combustion, and the n-Co0.2Ce0.8/SM (except for n=0.5) catalysts show higher catalytic ability than the unsupported Co_3O_4–CeO_2 particles, which are attributed to the net-like macropores structure of SM that can provide larger contact area between soot and catalytic active sites because the soot can enter into the inner pores. For 0.5-$Co_{0.2}Ce_{0.8}$/SM, the active components are mainly restricted in the mesoporous channels, which is not beneficial for the contact between the soot and the active components, thus the observed catalytic activity is poor. For the *n*-$Co_{0.2}Ce_{0.8}$/SM catalysts, with the increase of the *n* value, the catalytic activity is first increased but declined again at high *n* values due to the agglomeration of excess Co_3O_4–CeO_2 composite. Among them, 2-$Co_{0.2}Ce_{0.8}$/SM exhibits the best catalytic activity with the lowest T_{10} (293 ^oC), T_{50} (345 ^oC), and T_{90} (378 ^oC), mainly because of the high dispersion of Co_3O_4–CeO_2 on the outer surface of SM framework.

The catalytic activities of 2-Co_xCe_y/SM with different Co/Ce ratios were evaluated under O_2/NO atmosphere and their soot-TPO curves are shown in Fig. 8b. With the increase of *x:y* value, the catalytic activities of 2-Co_xCe_y/SM are firstly increased but subsequently decreased again. Among them, 2-$Co_{0.2}Ce_{0.8}$/SM exhibits the best catalytic activity with the lowest T_{10}, T_{50} and T_{90} as listed in Table 3. It reveals that the optimum Co/Ce molar ratio is at 1:4, and this result is consistent with the previous report.[17]

To further study the effect of NO as well as the contact condition between soot and catalyst on soot oxidation, the catalytic activities of 2-$Co_{0.2}Ce_{0.8}$/SM mixed with soot by spatula (loose contact) or under O_2 and NO/O_2 atmosphere were also evaluated and the results are shown in Fig. 8c. The soot combustion on the catalyst with loose contact obviously needs higher temperature as compared with the catalysts that are conducted with ultrasonic treatment. Clearly, the contact condition between soot and catalyst significantly influences the soot oxidation, and the ultrasonic treatment is

beneficial to the soot oxidation because it can make the soot particles well dispersed in the macropores of 2-$Co_{0.2}Ce_{0.8}$/SM. Under the loose contact condition, the TPO profile over 2-$Co_{0.2}Ce_{0.8}$/SM under only O_2 atmosphere shifts to higher temperature as compared with that under NO/O_2 atmosphere. Besides, we further compared soot combustion in O_2 with that in NO/O_2 atmosphere over SM under the loose contact condition, and the results are shown in Fig. 8c and Table S1. The two TPO profiles over SM under O_2 and NO/O_2 atmosphere are almost overlapped and show the same T_{10}, T_{50} and T_{90}, indicating that the introduction of NO_x has almost no influence on the combustion of soot over SM without Co_3O_4-CeO_2. Based on these results, it can be deduced that the Co_3O_4-CeO_2 species that help oxidize NO to NO_2, which has stronger oxidation ability than O_2 and subsequently oxidize the soot to CO_2. That is, it is able to subtly change solid (soot)–solid (catalyst) contact into solid (soot)–gas (NO_2)–solid (catalyst) contact.[12]

4. Conclusions

Cobalt and cerium oxides modified SBA-15 monolith (CoCe/SM) with different loadings and Co/Ce ratios are synthesized by the facile isovolumetric impregnation and their catalytic activities towards soot oxidation are evaluated. It is observed that 2-$Co_{0.2}Ce_{0.8}$/SM with the Co/Ce ratio of 1:4 exhibits the best catalytic activity with the lowest T_{10} (293 ^{o}C), T_{50} (345 ^{o}C), and T_{90} (378 ^{o}C) and highest selectivity to CO_2 (100%). This is attributed to the appropriate loading of Co_3O_4–CeO_2 and their high dispersion on the SM support with crosslinked micropores, which generate more exposed and efficient active sites. In addition, the macropores originated from the 3D network within SM can efficiently capture soot particulate and thus enhance the contact between the soot and the active sites of the catalyst. All these merits contribute to the improved catalytic soot oxidation activity of 2-$Co_{0.2}Ce_{0.8}$/SM.

Acknowledgments

The authors gratefully acknowledge the supports from the National Natural Science Foundation of China (No. 21206173).

References

1. T. Johnson, *Platinum Met. Rev.*, 2008, **52**, 23–37.
2. R. Prasad and V. R. Bella, *Bull. Chem. React. Eng. Catal*, 2010, **5**, 69–86.
3. Y. Teraoka, K. Kanada and S. Kagawa, *Appl. Catal., B*, 2001, **34**, 73–78.
4. B. S. Sanchez, C. A. Querini and E. E. Miro, *Appl. Catal., A*, 2009, **366**, 166–175.
5. K.-i. Shimizu, H. Kawachi, S.-i. Komai, K. Yoshida, Y. Sasaki and A. Satsuma, *Catal. Today*, 2011, **175**, 93–99.
6. C.-B. Lim, H. Kusaba, H. Einaga and Y. Teraoka, *Catal. Today*, 2011, **175**, 106–111.
7. B. He, Q. Song, Q. Yao, Z. Meng and C. Chen, *Korean J. Chem. Eng.*, 2007, **24**, 503–507.
8. X. Wu, R. Ran and D. Weng, *Catal. Lett.*, 2009, **131**, 494–499.
9. K. Wang, L. Qian, L. Zhang, H. Liu and Z. Yan, *Catal. Today*, 2010, **158**, 423–426.
10. X. Wu, S. Liu, D. Weng and F. Lin, *Catal. Commun.*, 2011, **12**, 345–348.
11. H. Muroyama, S. Hano, T. Matsui and K. Eguchi, *Catal. Today*, 2010, **153**, 133–135.
12. J. Liu, Z. Zhao, J. Wang, C. Xu, A. Duan, G. Jiang and Q. Yang, *Appl. Catal., B*, 2008, **84**, 185–195.
13. E. D. Banus, V. G. Milt, E. E. Miro and M. A. Ulla, *Appl. Catal., B*, 2013, **132**, 479–486.
14. H. Zhang, F. Gu, Q. Liu, J. Gao, L. Jia, T. Zhu, Y. Chen, Z. Zhong and F. Su, *RSC Adv.*, 2014, **4**, 14879–14889.
15. C.-W. Tang, C.-C. Kuo, M.-C. Kuo, C.-B. Wang and S.-H. Chien, *Appl. Catal., A*, 2006, **309**,

37–43.

16. Y. Zhou, W. G. Lin, J. Yang, L. Gao, N. Lin, J. Y. Yang, Q. Hou, Y. Wang and J. H. Zhu, *J. Colloid Interface Sci.*, 2011, **364**, 594–604.
17. M. Dhakad, T. Mitshuhashi, S. Rayalu, P. Doggali, S. Bakardjiva, J. Subrt, D. Fino, H. Haneda and N. Labhsetwar, *Catal. Today*, 2008, **132**, 188–193.
18. X. Wu, F. Lin, H. Xu and D. Weng, *Appl. Catal., B*, 2010, **96**, 101–109.
19. D. Zhao, J. Feng, Q. Huo, N. Melosh, G. H. Fredrickson, B. F. Chmelka and G. D. Stucky, *Sci.*, 1998, **279**, 548–552.
20. M. Skoglundh, H. Johansson, L. Löwendahl, K. Jansson, L. Dahl and B. Hirschauer, *Appl. Catal., B*, 1996, **7**, 299–319.
21. Y. Zhou, W. Qian, J. Yang, S. Zhou, Y. Wang and J. Zhu, *Chin. J. Chem.*, 2012, **30**, 2073-2078.
22. S. Todorova, G. Kadinov, K. Tenchev, A. Caballero, J. Holgado and R. Pereñíguez, *Catal. Lett.*, 2009, **129**, 149–155.
23. E. Beche, P. Charvin, D. Perarnau, S. Abanades and G. Flamant, *Surf. Interface Anal.*, 2008, **40**, 264–267.
24. M. Romeo, K. Bak, J. El Fallah, F. Le Normand and L. Hilaire, *Surf. Interface Anal.*, 1993, **20**, 508–512.
25. Y. Wei, J. Liu, Z. Zhao, A. Duan and G. Jiang, *J. Catal.*, 2012, **287**, 13–29.
26. L. Liotta, G. Di Carlo, G. Pantaleo, A. Venezia and G. Deganello, *Appl. Catal., B*, 2006, **66**, 217–227.
27. Z. Zhao, X. Yang and Y. Wu, *Appl. Catal., B*, 1996, **8**, 281–297.
28. T. Bao, Z. Zhao, Y. Dai, X. Lin, R. Jin, G. Wang and T. Muhammad, *Appl. Catal., B*, 2012, **119–120**, 62–73.

29. P. Gawade, B. Bayram, A.-M. C. Alexander and U. S. Ozkan, *Appl. Catal., B*, 2012, **128**, 21–30.

30. J.-Y. Luo, M. Meng, X. Li, X.-G. Li, Y.-Q. Zha, T.-D. Hu, Y.-N. Xie and J. Zhang, *J. Catal.*, 2008, **254**, 310–324.

31. R. Balzer, L. F. D. Probst, V. Drago, W. H. Schreiner and H. V. Fajardo, *Braz. J. Chem. Eng.*, 2014, **31**, 757–769.

Figure Captions

Fig. 1 N_2 adsorption-desorption isotherms (a) and PSD curves (b) of all the samples. (The isotherms for SM, 0.5-$Co_{0.2}Ce_{0.8}$/SM, 1-$Co_{0.2}Ce_{0.8}$/SM, 2-$Co_{0.2}Ce_{0.8}$/SM, 3-$Co_{0.2}Ce_{0.8}$/SM, 4-$Co_{0.2}Ce_{0.8}$/SM, and Co_3O_4–CeO_2 are offset vertically by 700, 600, 500, 400, 300, 200, and 100 cm^3/g STP, respectively.)

Fig. 2 SEM images of the SM (a), 0.5-$Co_{0.2}Ce_{0.8}$/SM (b), 1-$Co_{0.2}Ce_{0.8}$/SM (c), 2-$Co_{0.2}Ce_{0.8}$/SM (d), 3-$Co_{0.2}Ce_{0.8}$/SM (e), and 4-$Co_{0.2}Ce_{0.8}$/SM (f) (inset of (a) is the optical graph of SM and other insets are the magnified ones).

Fig. 3 SEM image of 2-$Co_{0.2}Ce_{0.8}$/SM (a), elemental mapping images of Si (b), O (c), Co (d), Ce (e), and SEM-EDX spectrum (f).

Fig. 4 TEM images of SM (a), 0.5-$Co_{0.2}Ce_{0.8}$/SM (b), 2-$Co_{0.2}Ce_{0.8}$/SM (c), 3-$Co_{0.2}Ce_{0.8}$/SM (d), 4-$Co_{0.2}Ce_{0.8}$/SM (e), and HRTEM image of 3-$Co_{0.2}Ce_{0.8}$/SM (f).

Fig. 5 Low-angle (a) and wide-angle (b) XRD patterns of all the samples.

Fig. 6 XPS spectrum of the Co_3O_4–CeO_2 and 2-$Co_{0.2}Ce_{0.8}$/SM catalysts: (a) wide spectrum , (b) Co 2p, (c) Ce 3d, and (d) O 1s.

Fig. 7 H_2-TPR (a) and O_2-TPD curves (b) of all the catalysts.

Fig. 8 Soot-TPO curves over the *n*-$Co_{0.2}Ce_{0.8}$/SM catalysts and Co_3O_4–CeO_2 under O_2/NO atmosphere (a), 2-Co_xCe_y/SM with different Co/Ce ratios under O_2/NO atmosphere (b), and 2-$Co_{0.2}Ce_{0.8}$/SM and SM under different reaction conditions (c).

Table 1 Physical-chemical properties of all the samples

Samples	S_{BET} [a]	V [b]	D [c]	Crystal size [d]	
	(m^2 g^{-1})	(cm^3 g^{-1})	(nm)	Co_3O_4/nm	CeO_2/nm
SM	617	0.65	7.7	—	—
Co_3O_4–CeO_2	50	0.059	3.4	14.3	6.4
0.5-$Co_{0.2}Ce_{0.8}$/SM	358	0.38	7.6	—	5.1
1-$Co_{0.2}Ce_{0.8}$/SM	280	0.30	7.6	12.8	5.7
2-$Co_{0.2}Ce_{0.8}$/SM	174	0.20	7.7	13.9	7.0
3-$Co_{0.2}Ce_{0.8}$/SM	130	0.16	7.7	13.7	8.8
4-$Co_{0.2}Ce_{0.8}$/SM	106	0.13	7.7	13.5	9.0

[a] S_{BET}, specific surface area determined by BET method;

[b] *V*, Pore volume obtained from the volume of nitrogen adsorbed at the relative pressure of 0.97;

[c] *D*, Pore size derived from BJH method using adsorption branch;

[d] Crystal size, derived from XRD by Debye-Scherrer equation.

Table 2 Surface composition and oxidation state of Ce and O species derived from XPS analyses

Catalysts	Ce species			O species		
	Ce^{3+}	Ce^{4+}	R_1[a]	O_2^- and O^-	O^{2-}	R_2[b]
Co_3O_4–CeO_2	21.1	78.9	0.267	32.0	68.0	0.471
2-$Co_{0.2}Ce_{0.8}$/SM	23.0	77.0	0.299	54.0	46.0	1.17

[a] R_1, determined by the Ce molar ratio of the Ce^{3+}/Ce^{4+}.

[b] R_2, determined by the oxygen species ratio of the adsorbed oxygen (O^-+ O_2^-)/lattice oxygen (O^{2-}).

Table 3 The temperatures and the selectivity to CO_2 for soot combustion over without catalyst, SM, the *n*-Co_xCe_y/SM, and unsupported Co_3O_4–CeO_2.

Catalysts	T_{10} (°C)	T_{50} (°C)	T_{90} (°C)	S_{CO_2} (%)
Soot	447	563	612	55
SM support	445	563	610	50
0.5- $Co_{0.2}Ce_{0.8}$ /SM	325	392	429	100
1- $Co_{0.2}Ce_{0.8}$ /SM	308	358	389	99.9
2- $Co_{0.1}Ce_{0.9}$ /SM	306	365	400	100
2- $Co_{0.2}Ce_{0.8}$ /SM	293	345	378	100
2- $Co_{0.3}Ce_{0.7}$ /SM	304	365	410	100
2- $Co_{0.5}Ce_{0.5}$ /SM	307	361	403	100
3- $Co_{0.2}Ce_{0.8}$ /SM	311	368	405	100
4- $Co_{0.2}Ce_{0.8}$ /SM	313	362	398	99.82
Co_3O_4–CeO_2	308	369	412	100

Reaction conditions: reaction gas, 10% O_2 and 0.1% NO in Ar, 50 mL min^{-1}; the soot/catalyst mass ration is 1/20.

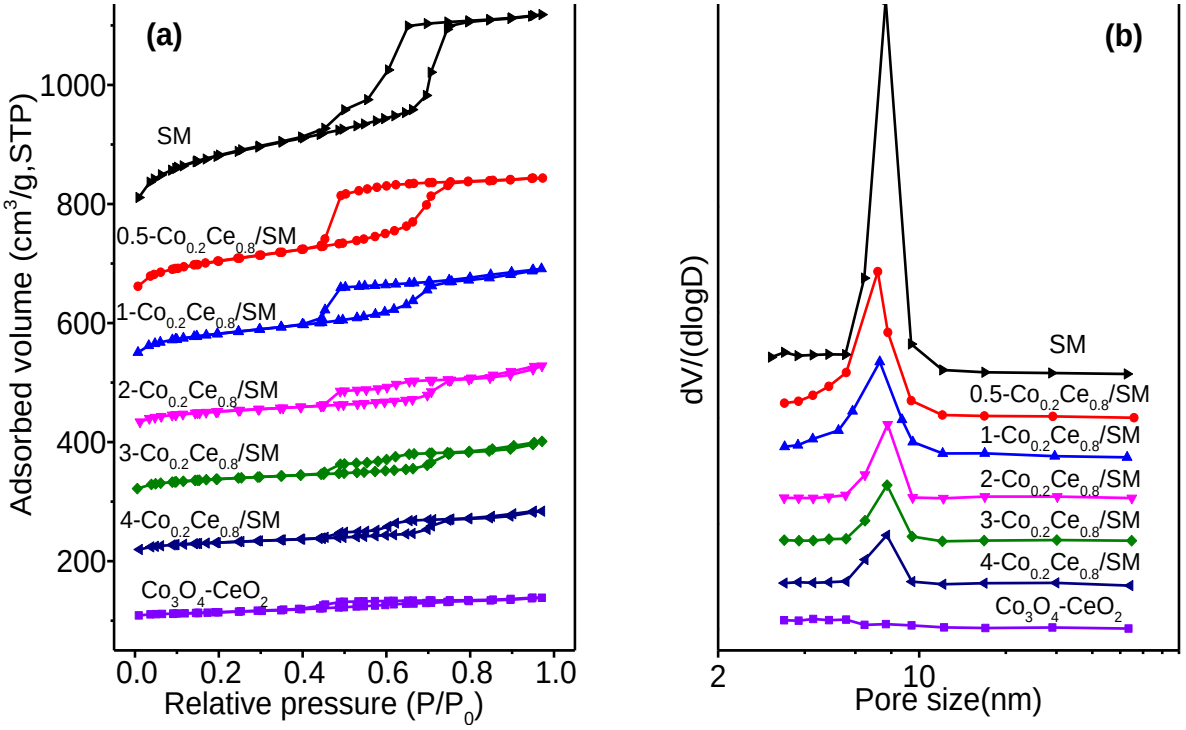

Fig. 1

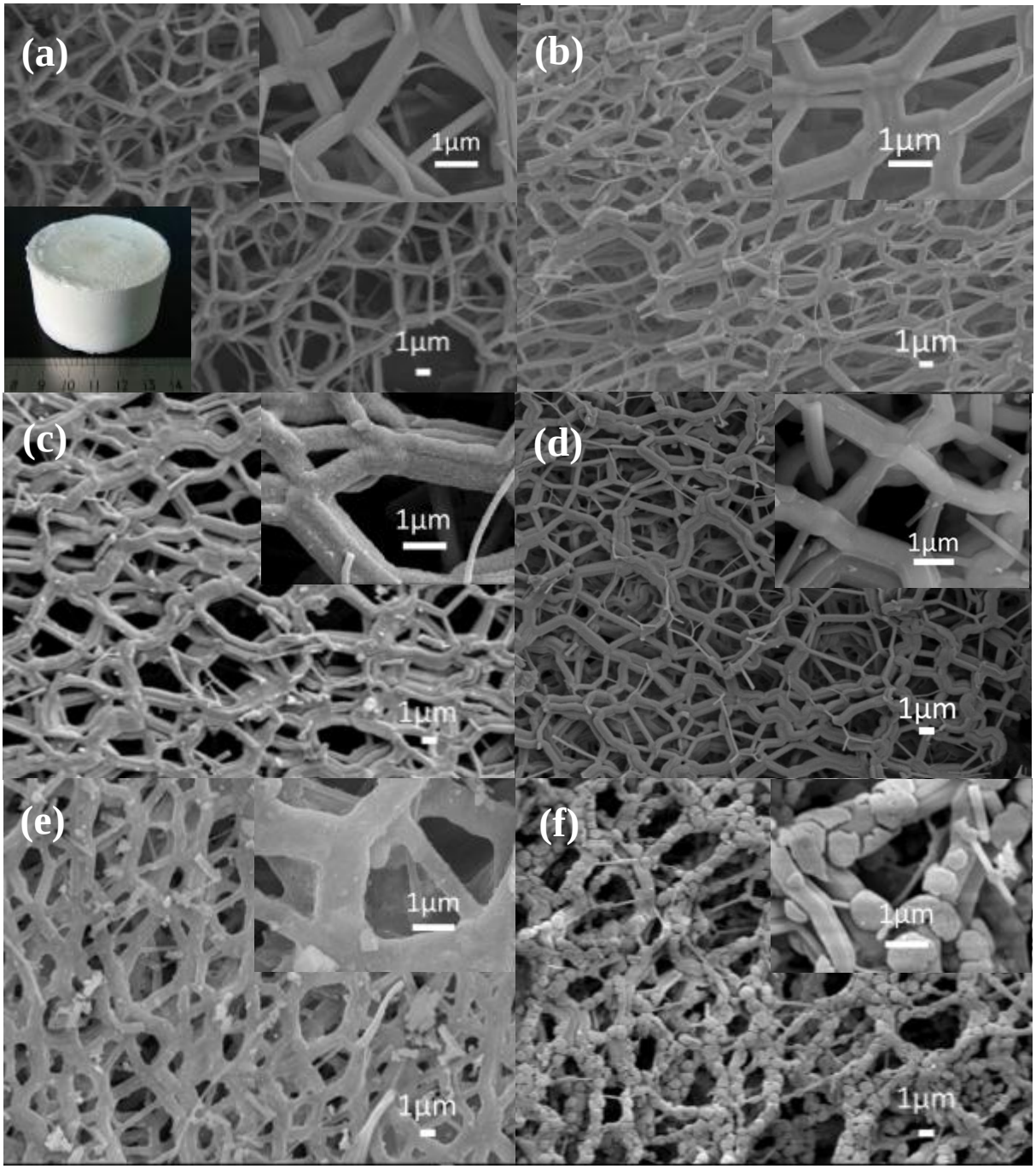

Fig. 2

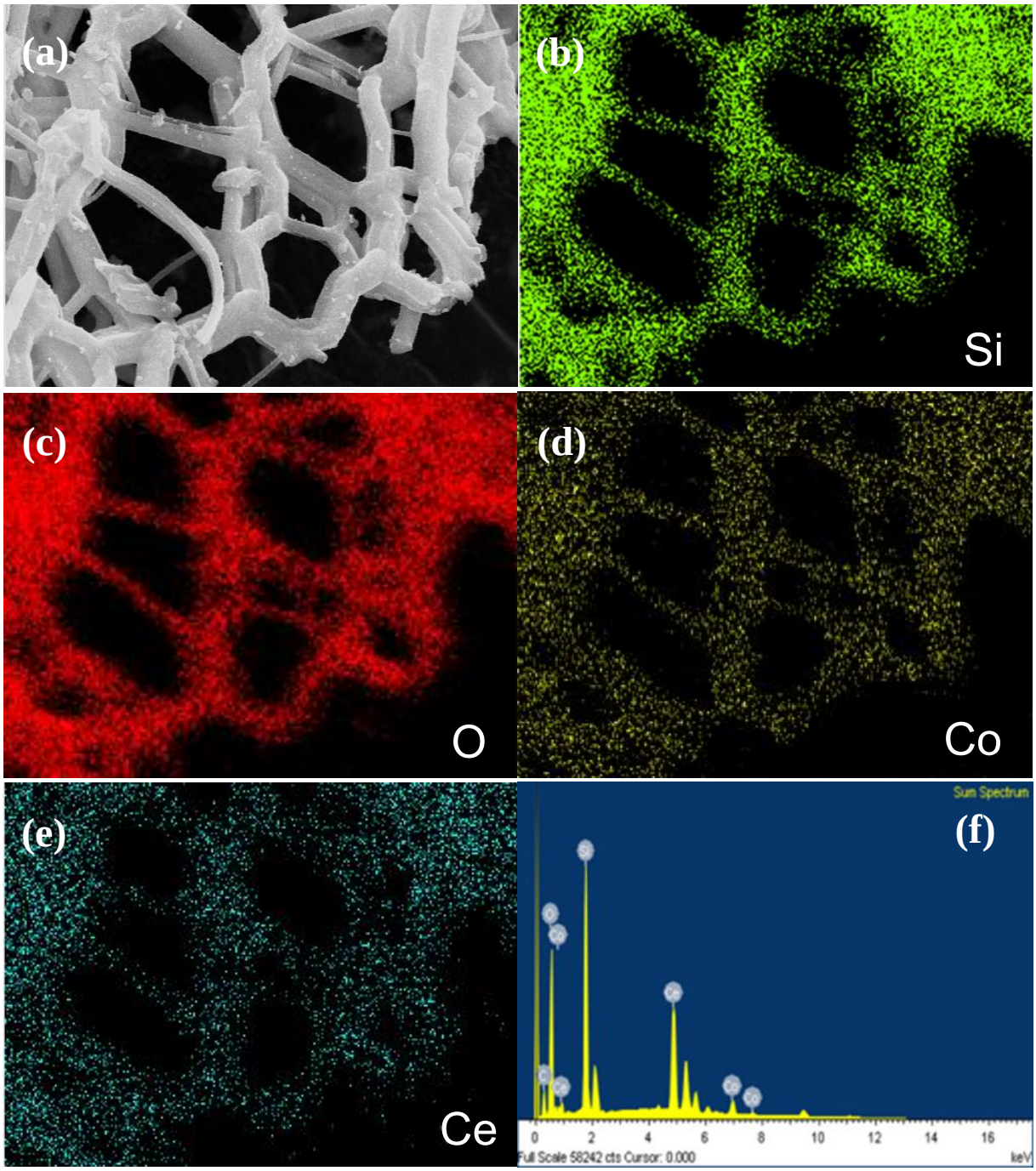

Fig. 3

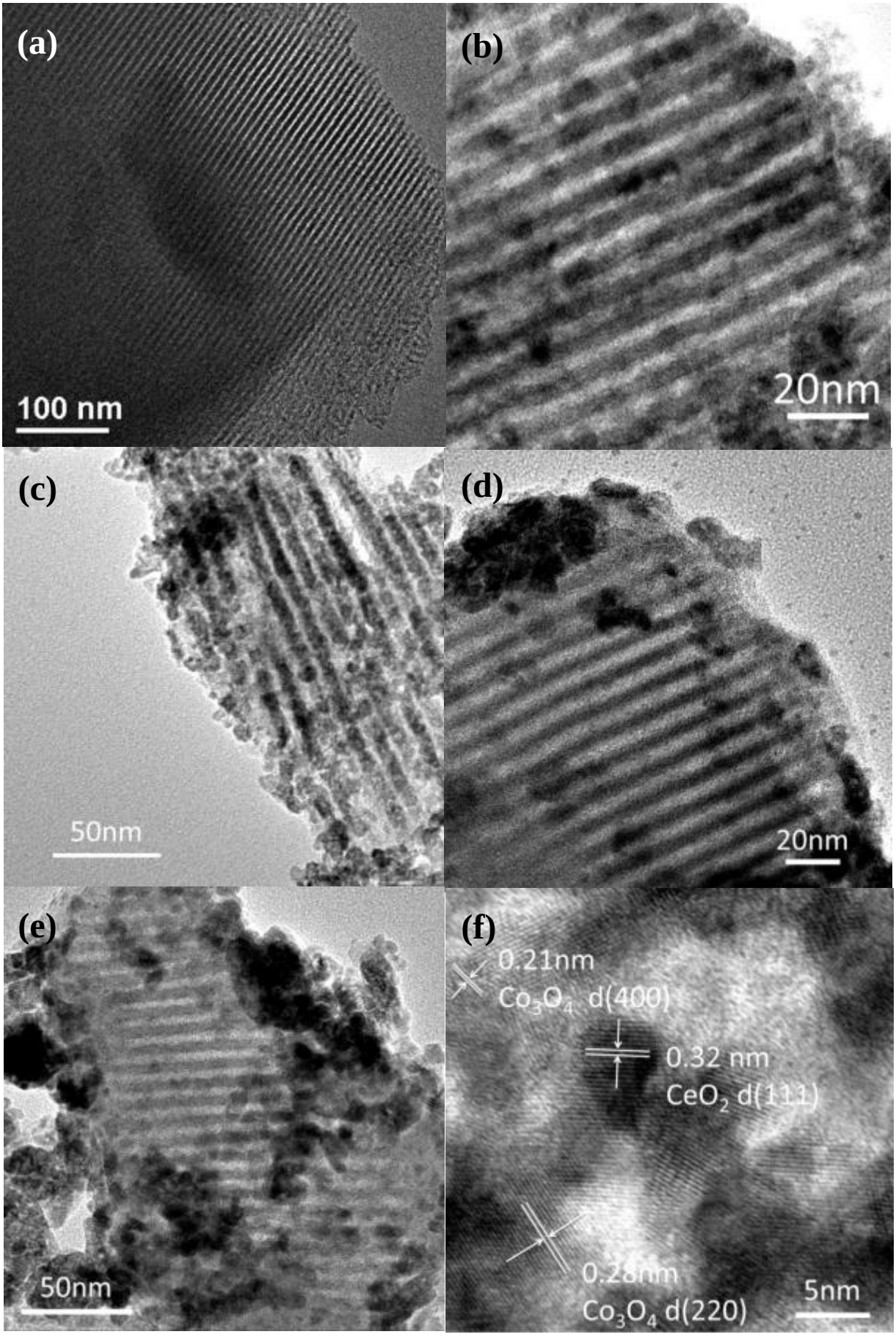

Fig. 4

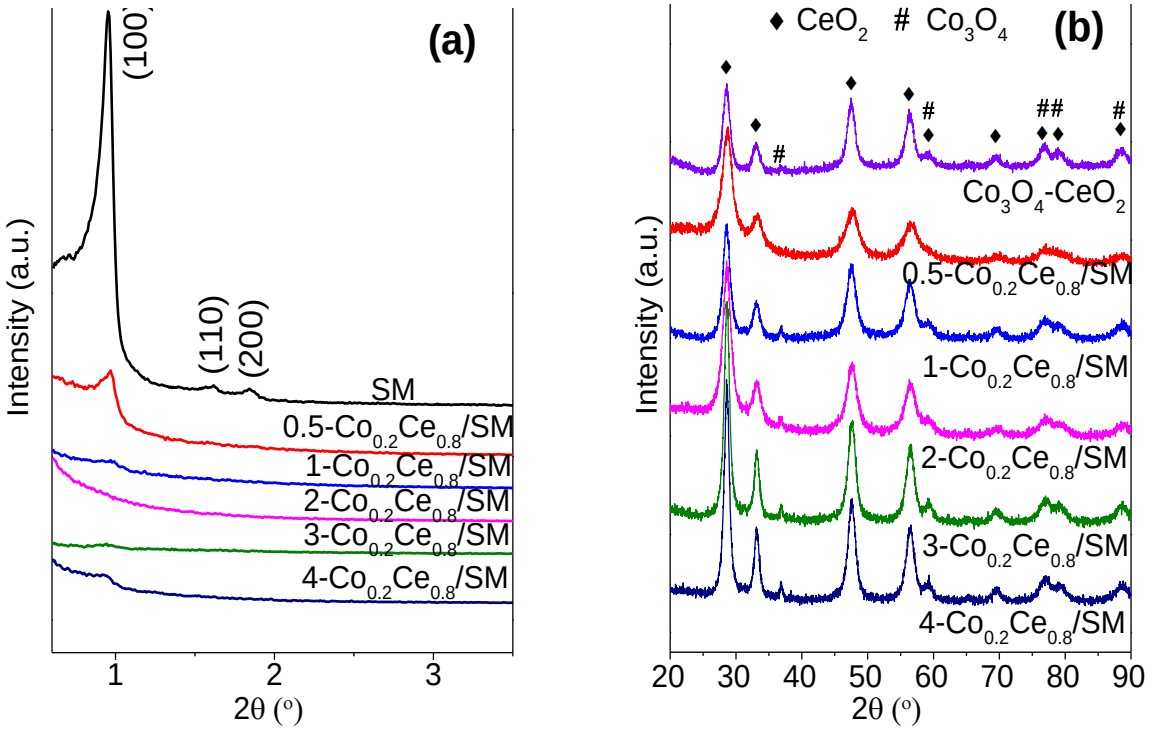

Fig. 5

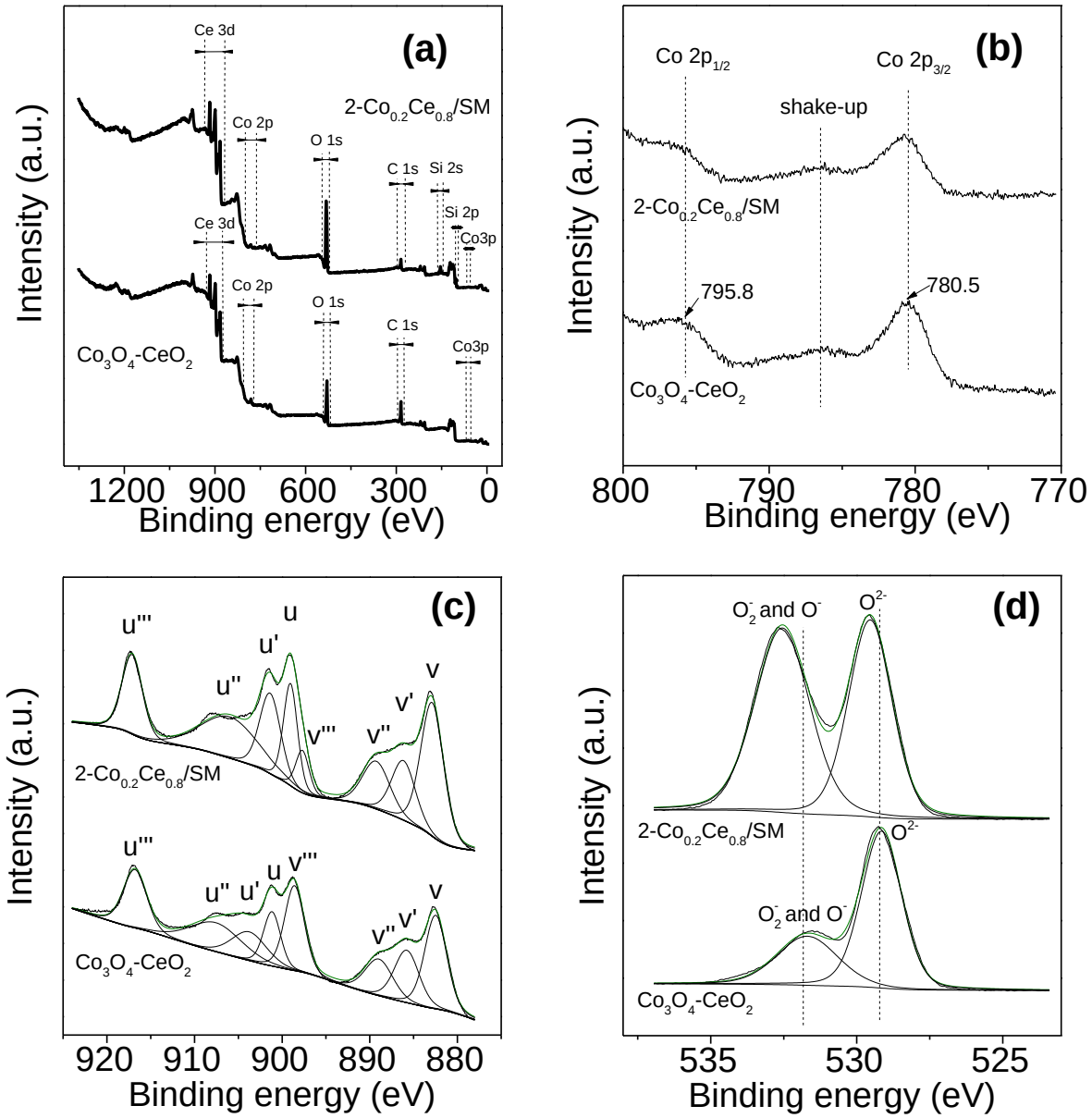

Fig. 6

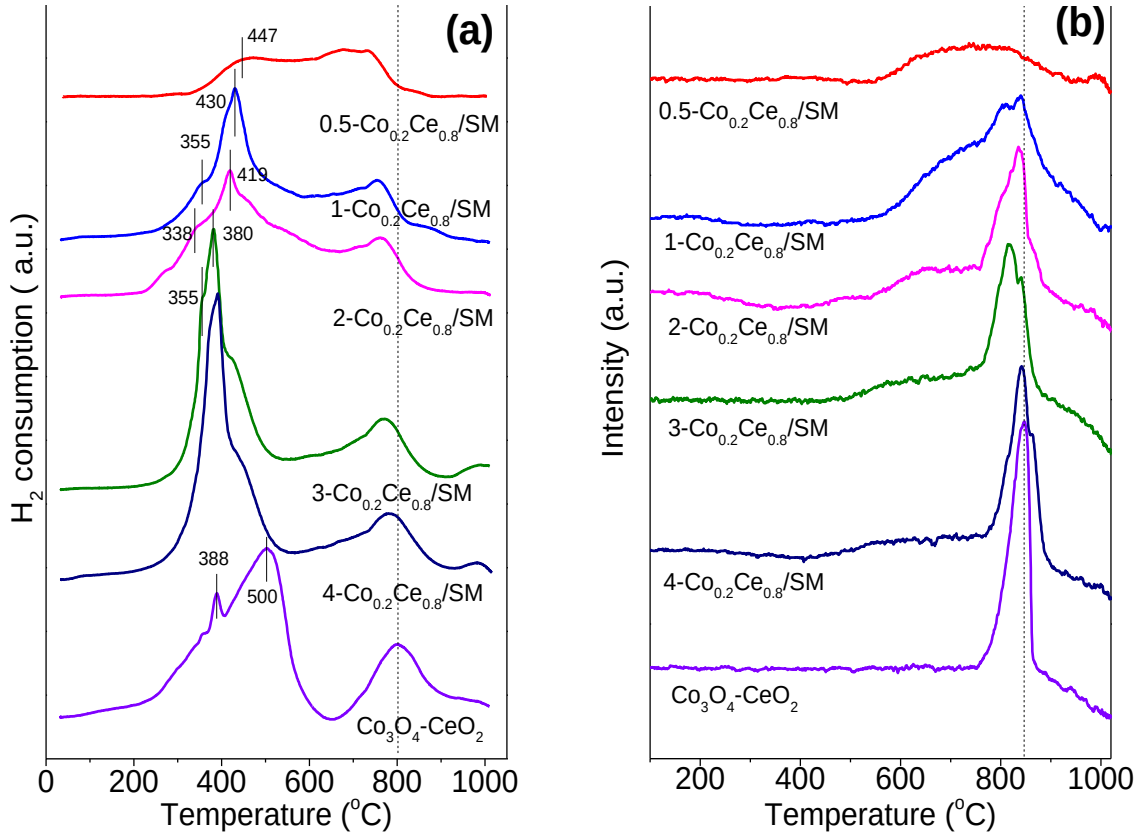

Fig. 7

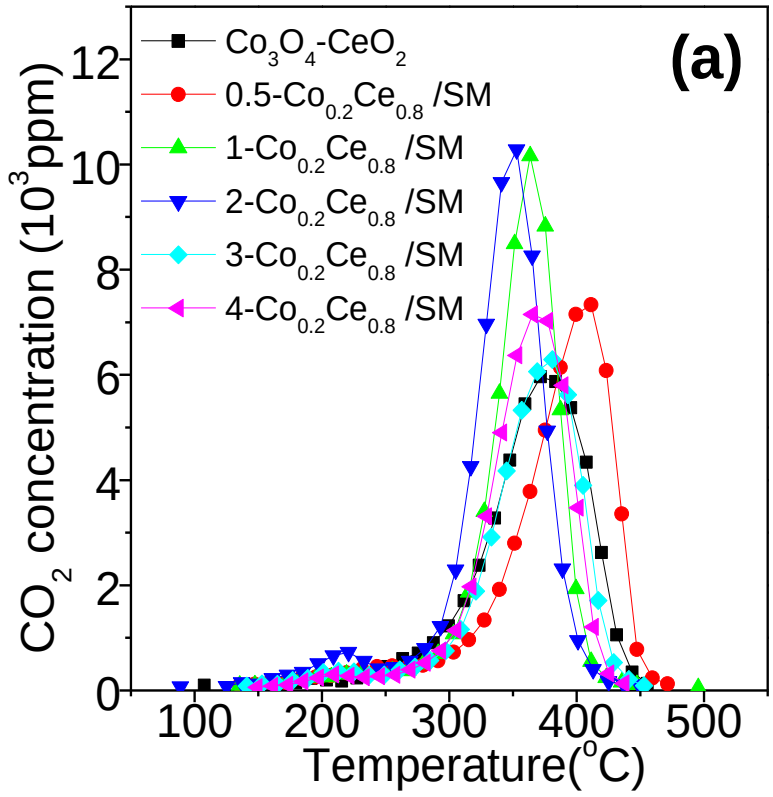

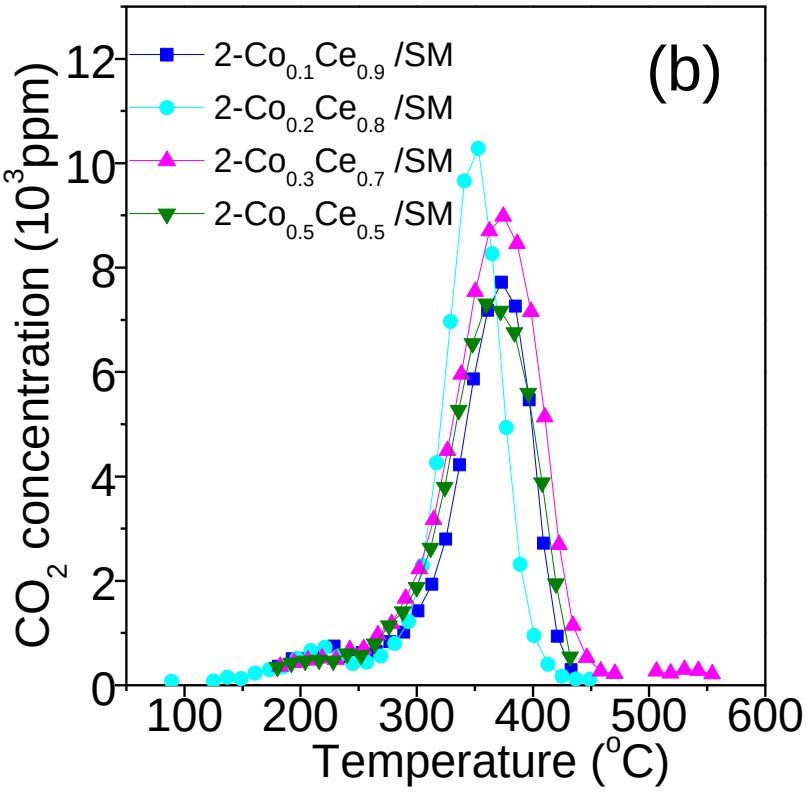

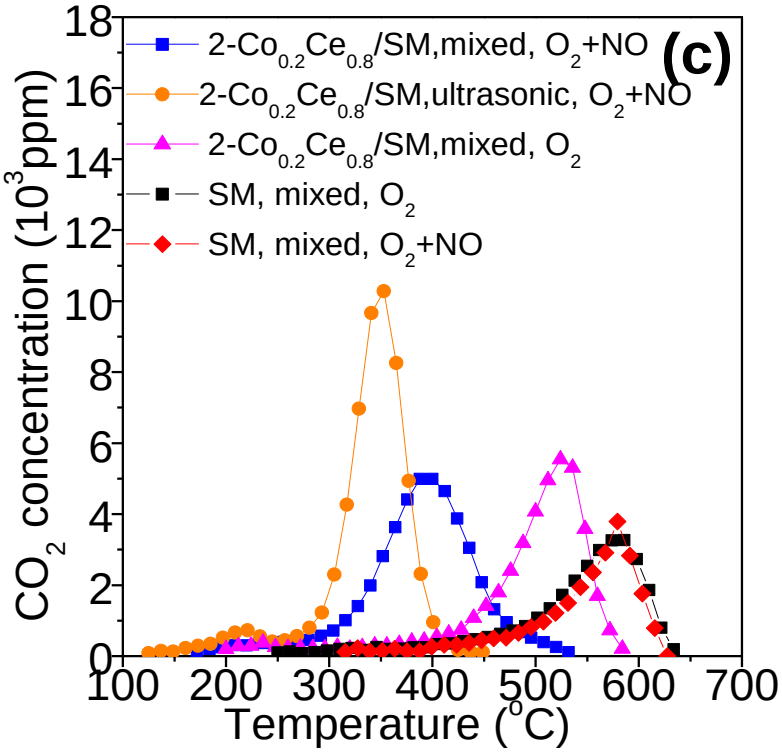

Fig. 8